







# Impairments in endogenous AMPA receptor dynamics correlates with learning deficits in Alzheimer's disease model mice

Kongjie Lu<sup>ab</sup>, Chenyang Li<sup>ab</sup>, Jiao Liu<sup>c</sup>, Jinpeng Wang<sup>ab</sup>, Yongfeng Li<sup>ab</sup>, Bin He<sup>ab</sup>, Junzhao Li<sup>ab</sup>, Xiaochen Zhang<sup>d</sup>, Mengping Wei<sup>e</sup>, Yonglu Tian<sup>bf</sup> , Rong Zhang<sup>ab</sup> , Chen Zhang<sup>e</sup> , and Yong Zhang<sup>ab,1</sup> 

Edited by Jeremy Nathans, Johns Hopkins University School of Medicine, Baltimore, MD; received March 27, 2023; accepted August 29, 2023

AMPA receptors (AMPA) play a critical role in synaptic plasticity and learning and memory, and dysfunction or dysregulation of AMPARs could lead to various neurological and psychiatric disorders, such as Alzheimer's disease (AD). However, the dynamics and/or longitudinal changes of AMPARs in vivo during AD pathogenesis remain elusive. Here, employing 5xFAD SEP-GluA1 KI mice, we investigated endogenous AMPA receptor dynamics in a whisker deflection-associated Go/No-go learning paradigm. We found a significant increase in synaptosomal AMPA receptor subunits GluA1 in WT mice after learning, while no such changes were detected in 7-mo-old 5xFAD mice. Daily training led to an increase in endogenous spine surface GluA1 in Control mice, while this increase was absent in 5xFAD-KI mice which correlates with its learning defects in Go/No-go paradigm. Furthermore, we demonstrated that the onset of abnormal AMPAR dynamics corresponds temporally with microglia and astrocyte overactivation. Our results have shown that impairments in endogenous AMPA receptor dynamics play an important role in learning deficits in 5xFAD mice and AD pathogenesis.

AMPA receptor | synaptic plasticity | two-photon imaging | Alzheimer's disease

$\alpha$ -amino-3-hydroxy-5-methyl-4-isoxazole propionic acid receptors (AMPA) mediate the majority of excitatory neurotransmission in the brain and thus play a critical role in many aspects of brain function, including cognition, movement, learning, and memory. The insertion and removal of AMPARs from the postsynaptic site mediate long-term potentiation (LTP) and long-term depression, respectively (1–7). Dysregulation or impairments of AMPA receptor function could lead to a variety of neurological and psychiatric disorders, such as Alzheimer's disease (AD) (8, 9). AD is a neurodegenerative disorder characterized by memory deficits and cognitive decline. Three well-established pathological hallmarks of AD are amyloid- $\beta$  (A $\beta$ ) plaques, neurofibrillary tangles (NFT), and neuronal loss (10–14). AD is a progressive disorder, where dementia symptoms gradually worsen over a number of years. Autopsy studies have shown that people with AD tend to develop far more plaques and tangles and in a predictable pattern, which begins in areas that affect learning and memory and then spreads to other regions as the disease progresses. Accumulating evidence has suggested that one of the earliest manifestations in AD is probably the decrease of synaptic AMPA receptors and abnormalities in synaptic plasticity (15–17). Multiple studies have demonstrated that abnormal AMPA receptor function is closely associated with cognitive impairments in AD (10, 17–21).

Previous in vitro studies have greatly advanced our knowledge of AMPA receptor trafficking and regulation at the molecular level. Recently, utilizing two-photon microscopy, people have investigated AMPA receptor dynamics in vivo (22–26) and found that daily training leads to an increase in AMPA receptor level at a subset of spatially clustered dendritic spines in the motor cortex in a forelimb reaching task (24). However, exogenous overexpression of SEP-tagged AMPARs may result in protein mistargeting and dysregulation. To overcome this caveat, the Haganir group has utilized novel genetic labeling strategy and created a SEP-GluA1 knockin mouse line, which enables longitudinal tracking of endogenous AMPAR dynamics in a manner that does not impair synaptic function (27). However, very few studies have been conducted to investigate AMPA receptor dynamics in real time in AD animals. More than 100 transgenic AD lines have been generated and display different phenotypes depending on the transgene, such as APP<sup>swe</sup>/PS1, 3xTg, 5xFAD, and APP<sup>swe</sup>, among which 5xFAD is most commonly used (28). 5xFAD mice express the Swedish (APPK670N/M671L), London (APPV717I), and Florida (APP1716V) mutations in APP and the PS1M146L and PS1L286V mutations in PSEN1 (29). Amyloid pathology starts at 2 mo of age in 5xFAD mice, including amyloid plaques (29). Age-dependent memory deficits, including spatial memory, stress-related memory and memory stabilization, are the major phenotypes in 5xFAD (29–33). Considering the time

## Significance

Dysregulation of AMPA receptors (AMPA) contributes to a number of neurological and psychiatric disorders, including AD. However, studying longitudinal AMPAR changes in AD animals has been a big challenge, to tackle this problem, we crossed fluorescently tagged AMPAR subunit GluA1 knockin mice with AD model mice, 5xFAD, and investigated endogenous GluA1 dynamics in a Go/No-go learning paradigm. Our results showed that impairments in AMPAR dynamics and microglia/astrocytes overactivation surrounding A $\beta$  plaques correlate with learning deficits in AD animals. Our study observed endogenous AMPAR dynamics in real time in AD mice during learning which provides hints for better understanding of AD pathogenesis.

Author contributions: K.L., R.Z., C.Z., and Y.Z. designed research; K.L., C.L., J. Liu, J.W., Y.L., B.H., J. Li, X.Z., M.W., and Y.T. performed research; K.L. analyzed data; and K.L. and Y.Z. wrote the paper.

The authors declare no competing interest.

This article is a PNAS Direct Submission.

Copyright © 2023 the Author(s). Published by PNAS. This article is distributed under [Creative Commons Attribution-NonCommercial-NoDerivatives License 4.0 \(CC BY-NC-ND\)](https://creativecommons.org/licenses/by-nc-nd/4.0/).

<sup>1</sup>To whom correspondence may be addressed. Email: yongzhang@hsc.pku.edu.cn.

This article contains supporting information online at <https://www.pnas.org/lookup/suppl/doi:10.1073/pnas.2303878120/-/DCSupplemental>.

Published September 25, 2023.

until onset of phenotype, costs, and the consistency of pathology, we chose 5xFAD mice for our study.

To investigate endogenous AMPA receptor dynamics in AD animals, we crossed 5xFAD mice with SEP-GluA1 knockin mice to generate 5xFAD SEP-GluA1 hybrid mice (*Materials and Methods*) and employed whisker stimulation-associated Go/No-go behavioral paradigm to explore AMPA receptor changes longitudinally in real time during learning. We found that 7-mo-old 5xFAD mice displayed impaired learning ability, there were significant increases in synaptosomal AMPA receptor subunits GluA1 and GluA2 and N-methyl-D-aspartate receptor (NMDA receptor) subunits GluN2A and GluN2B in 7-mo-old wild type (WT) mice after learning, while no such increase was detected in age-matched 5xFAD mice. In vivo two-photon imaging results showed spine surface GluA1 (sGluA1) and spine size were all significantly increased in 7-mo-old Control mice during learning, while these changes were absent in age-matched 5xFAD-KI mice. The changes of surface GluA1 in individual spines were highly heterogeneous. Furthermore, we found that the impairments in GluA1 trafficking in 5xFAD mice during learning could be due to overactivation of microglia and astrocytes surrounding A $\beta$  plaques. Our findings suggest that impairments in endogenous AMPAR dynamics play an important role in learning deficits in 5xFAD mice.

## Results

**Seven-Month-Old 5xFAD Mice Displayed Impaired Learning Ability.** The 5xFAD mice rapidly develop severe amyloid pathology, in which extracellular amyloid deposition begins around 2 mo, first in the subiculum and layer V of the cortex, and accumulates quickly with age. Plaques have been found throughout the hippocampus and cortex by 6 mo (29). Impaired spatial memory in Morris water maze test was reported in 6-mo-old mice, and impaired learning was evident in 9-mo-old mice (30, 34). Learning ability of 6-mo-old 5xFAD mice was first accessed in a Go/No-go paradigm (*Materials and Methods*), mice were trained to perform the task in which they either lick or withhold licking depends on whether their whiskers received a brief deflection (Fig. 1*A* and *Movie S1*). There were four possible outcomes: successful detections (“Hits”) and failed detections (“Misses”) following the delivery of stimulus with big amplitude (16-degree radius) on Go trial, as well as “Correct Rejection” and “False Alarms” when stimulus with small amplitude was delivered (8-degree radius) on No-go trial (Fig. 1*B*). Mice performance (fraction correct) was assessed by the sum of hits and correct rejection trials divided by total number of trials. Mice were considered experts when performance reached  $\geq 70\%$  correct for two consecutive days and training would be stopped, and memory tests were performed a week after the last training session (Fig. 1*C*).

When 6-mo-old WT and 5xFAD mice were subjected to Go/No-go learning paradigm, on average, WT mice became experts of the task after 6 d of training, and 5xFAD mice also reached expert level on day 6 (Fig. 1*D* and *E*). As shown in Fig. 1*E* and *F*, there were no significant differences in sensory-associated learning ability and memory performance between WT and 5xFAD mice at 6 mo of age. We next subjected 7-mo-old animals to Go/No-go learning paradigm and found that WT mice reached expert level after 6 d of training, while it took  $\sim 9$  d for 5xFAD mice to reach expert level (Fig. 1*G* and *H*). When took a closer look, we found that 64.29% of the WT mice mastered the task on day 6, while only 18.75% of the 5xFAD mice mastered the task on day 6 (Fig. 1*I*). Interestingly, there were no significant differences between 7-mo-old WT and 5xFAD mice in memory test (Fig. 1*J*). These results suggest that 5xFAD mice displayed impaired learning ability at 7 mo of age.

**Increases in Synaptosomal AMPA and NMDA Receptors after Learning Were Absent in 7-Mo-Old 5xFAD Mice.** Abnormal changes in the number or function of AMPARs have been shown to be a core feature of age-related cognitive decline. To explore the changes of synaptic proteins in the Go/No-go paradigm after learning, we first measured levels of AMPARs in the primary somatosensory cortex (S1BF) via Western blot (Fig. 2*A* and *B* and *SI Appendix, Fig. S1 A and B*). There were significant increases in the levels of the synaptosomal GluA1 and GluA2 in both 6- and 7-mo-old WT mice after training (Fig. 2*A* and *B*). A significant increase in the synaptosomal GluA1 level was apparent in 6-mo-old 5xFAD mice after training, while no such increase was observed in 7-mo-old 5xFAD mice (Fig. 2*A* and *B*). Since NMDA receptors also play an important role in learning and memory, we next investigated changes of NMDA receptor subunits after Go/No-go training (Fig. 2*A* and *B* and *SI Appendix, Fig. S1 A and B*). No differences were detected in synaptosomal GluN1, GluN2A, and GluN2B levels between 6-mo-old WT and 5xFAD mice after training (Fig. 2*A*). There was a significant increase in synaptosomal GluN2A and GluN2B levels in 7-mo-old WT mice after learning, while no such changes were found in 7-mo-old 5xFAD mice (Fig. 2*B*).

It has been well documented that phosphorylation of GluA1 plays critical roles in AMPA receptor function and trafficking, so next we investigated the phosphorylation level of GluA1 (Fig. 2*C* and *SI Appendix, Fig. S1C*). Phosphorylation levels of synaptosomal GluA1 at both S831 and S845 were significantly increased in 6-mo-old WT and 5xFAD mice after training but not in 7-mo-old WT or 5xFAD mice (Fig. 2*C*). Studies have shown that CaMKII regulates many synaptic proteins that modulate excitatory transmission and synaptic function. PSD-95, a major component of the postsynaptic density (PSD), is involved in stabilization and trafficking of AMPA and NMDA receptors to the postsynaptic membrane. When we took a look at changes of these molecules, we found that the phosphorylation level of synaptosomal CaMKII- $\alpha$  was significantly increased in 6-mo-old WT and 5xFAD mice after training, while no such changes were detected between 7-mo-old WT and 5xFAD mice (Fig. 2*D* and *SI Appendix, Fig. S1D*). There were no significant changes in the synaptosomal PSD-95 protein levels before and after training in both 6- and 7-mo-old WT and 5xFAD mice (Fig. 2*E* and *SI Appendix, Fig. S1E*). These results show that the postsynaptic GluA1 level correlates with the learning ability in whisker stimulation-related Go/No-go task.

Western blots results showed that learning induced increases in AMPAR phosphorylation and CaMKII phosphorylation were absent in both 7-mo-old WT and 5xFAD mice, which indicates no correlation between learning ability and phosphorylation status. However, western blots could only assess changes of all neurons in the hippocampus or barrel cortex, thus could not rule out the possibility that CaMKII and GluA1 phosphorylation might be different at spine/synapse level after training between 7-mo-old WT and 5xFAD mice. To have a better understanding of AMPAR dynamics at individual spine/synapse level after training, we next performed two-photon imaging to investigate real time changes in live animals.

**Learning-Associated Whisker Stimulation Induces an Increase in Spine Size in Control but not 5xFAD-KI Mice.** To have a better understanding of the real-time changes of endogenous GluA1 during learning, we crossed 5xFAD mice with SEP-GluA1 knockin mice (27) to generate hybrid mice (5xFAD-KI, *Materials and Methods*) and utilized two-photon in vivo imaging to monitor AMPA receptor dynamics in Go/No-go paradigm. Since AMPA receptors express in almost all neurons in the brain, viruses carrying dsRed2 marker were injected into layer 2/3 of barrel cortex to

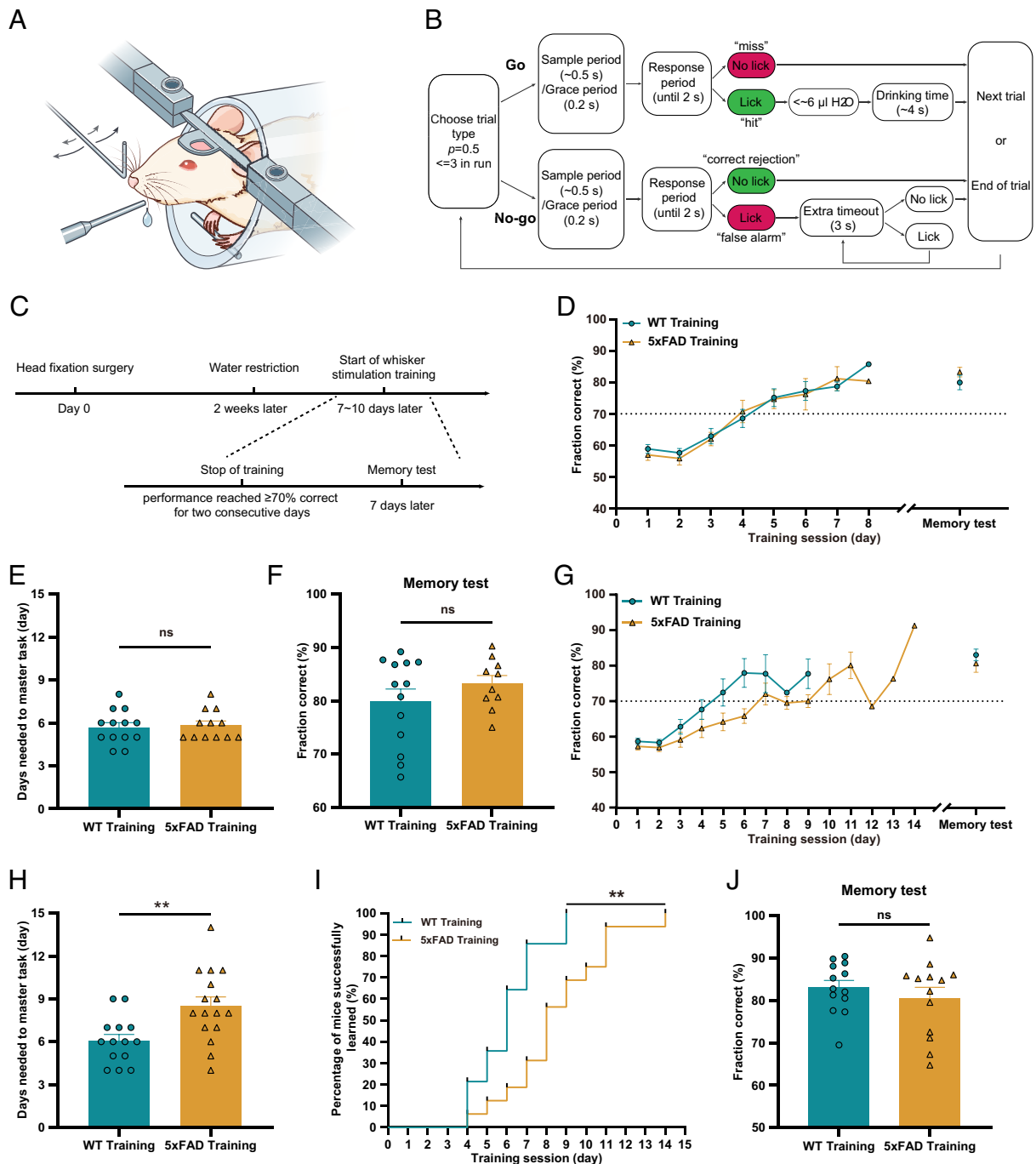


**Fig. 1.** Seven-month-old 5xFAD mice displayed impaired learning ability. (A) A side view of the Go/No-go task with the pole position and lickport. (B) Diagram of the sequence of events for a single trial (*Materials and Methods*). (C) Experimental timeline. (D) Learning curves of 6-mo-old mice in Go/No-go paradigm.  $n = 13$  (WT Training group),  $n = 12$  (5xFAD Training group). (E) Days needed for 6-mo-old mice to master the Go/No-go task.  $n = 13$  (WT Training group),  $n = 12$  (5xFAD Training group). (F) Behavioral performance of 6-mo-old mice at memory test.  $n = 13$  (WT Training group),  $n = 10$  (5xFAD Training group, two mice were excluded due to health problems). (G) Learning curves of 7-mo-old mice in Go/No-go paradigm.  $n = 14$  (WT Training group),  $n = 16$  (5xFAD Training group). (H) Days needed for 7-mo-old mice to master the Go/No-go task.  $n = 14$  (WT Training group),  $n = 16$  (5xFAD Training group). (I) Correlation plot between the percentage and number of days required to master the task in 7-mo-old mice.  $n = 14$  (WT Training group),  $n = 16$  (5xFAD Training group). Data are plotted as a tick symbol (staircases) without error bars. (J) Behavioral performance of 7-mo-old mice at memory test.  $n = 13$  (WT Training group, one mouse was excluded due to health problems),  $n = 13$  (5xFAD Training group, three mice were excluded due to health problems). Data are presented as mean  $\pm$  SEM. ns, not significant; \* $P < 0.05$ ; \*\* $P < 0.01$ ; Mann-Whitney  $U$  test (E); unpaired two-tailed  $t$  test (F, H, and J); Log-rank (Mantel-Cox) test (I).

sparsely label a subpopulation of pyramidal neurons to increase contrast in our imaging study (*SI Appendix, Fig. S2 A–D*). Mice were trained for five consecutive days, and memory was tested on day 12, two-photon imaging was conducted on the day before training starts and on training day 1, day 3, day 5, and day 12 (Fig. 3A). Consistent with our previous results, Control mice reached experts level on days 4 to 5 after training ( $70.87 \pm 2.814\%$ ,

$84.03 \pm 4.91\%$ , respectively), while 5xFAD-KI mice failed to do so ( $61.63 \pm 4.45\%$ ,  $68.53 \pm 8.221\%$ , respectively) (Fig. 3B). There were no significant differences between these two groups in memory test (Fig. 3C). Spine dynamics provide a structural basis for information storage in the brain, and spine turnover plays an important role in synaptic plasticity (35–38). So, we first investigated spine turnover during Go/No-go learning paradigm

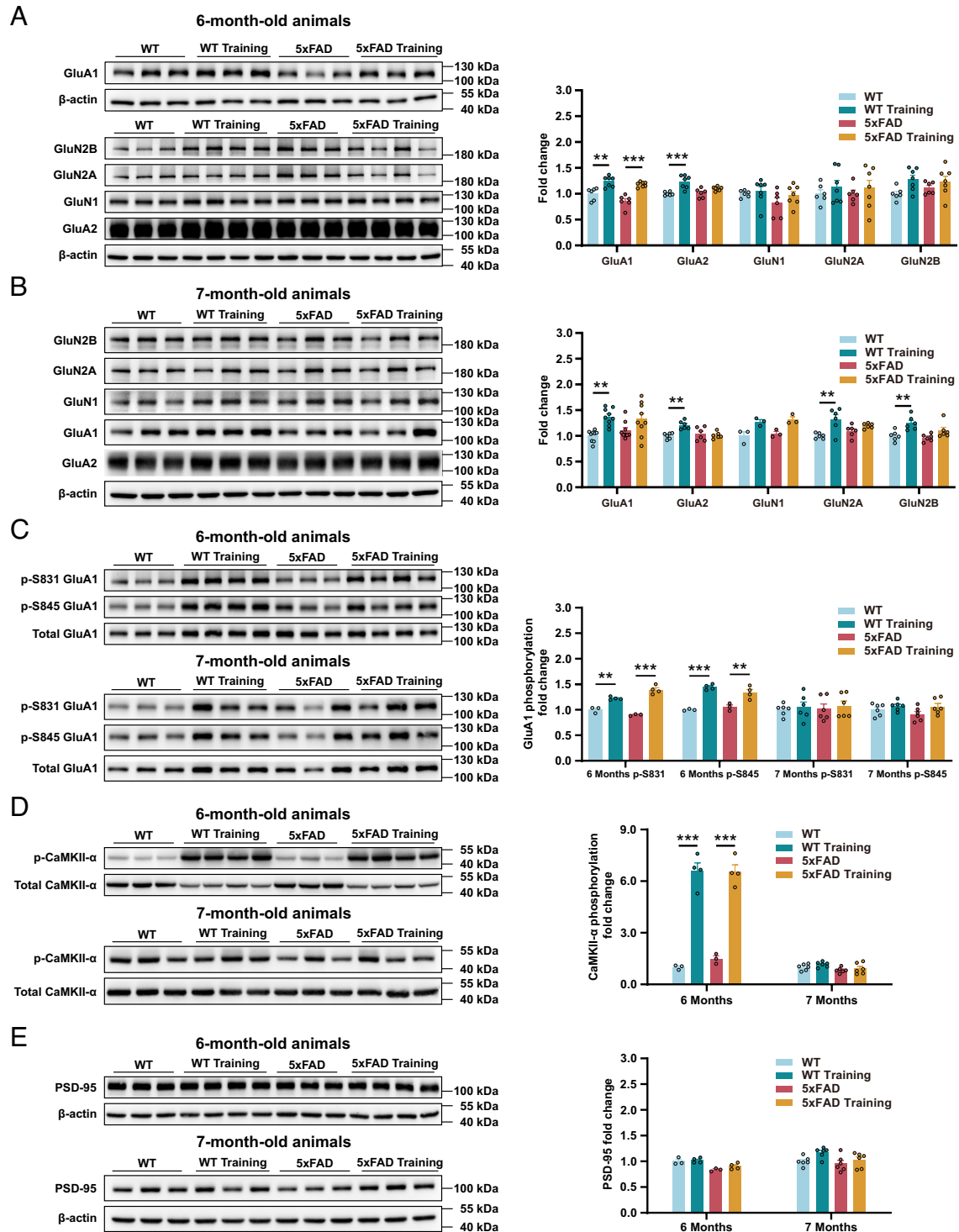


**Fig. 2.** Increases in synaptosomal AMPA and NMDA receptors after learning were absent in 7-mo-old 5xFAD mice. (A) Representative images of Western blots and quantification of synaptosomal AMPA and NMDA receptor levels in the S1BF of 6-mo-old mice before ( $n = 6$  each, WT or 5xFAD group) and after training ( $n = 7$  each, WT or 5xFAD Training group). (B) Representative images of Western blots and quantification of synaptosomal AMPA and NMDA receptor levels in the S1BF of 7-mo-old mice before ( $n = 6$  each, WT or 5xFAD group) and after training ( $n = 6$  each, WT or 5xFAD Training group). The number of mice in GluA1 is 9 ( $n = 9$ ) and GluN1 is 3 ( $n = 3$ ). (C) Representative images of Western blots and quantification of phosphorylation levels of synaptosomal GluA1 in the S1BF of 6- and 7-mo-old mice before ( $n = 3$  each, 6-mo-old WT or 5xFAD group;  $n = 6$  each, 7-mo-old WT or 5xFAD group) and after training ( $n = 4$  each, 6-mo-old WT or 5xFAD Training group;  $n = 6$  each, 7-mo-old WT or 5xFAD Training group). (D) Representative images of Western blots and quantification of phosphorylation levels of synaptosomal CaMKII- $\alpha$  in the S1BF of 6- and 7-mo-old mice before ( $n = 3$  each, 6-mo-old WT or 5xFAD group;  $n = 6$  each, 7-mo-old WT or 5xFAD group) and after training ( $n = 4$  each, 6-mo-old WT or 5xFAD Training group;  $n = 6$  each, 7-mo-old WT or 5xFAD Training group). (E) Representative images of Western blots and quantification of phosphorylation levels of synaptosomal PSD-95 levels in the S1BF of 6- and 7-mo-old mice before ( $n = 3$  each, 6-mo-old WT or 5xFAD group;  $n = 6$  each, 7-mo-old WT or 5xFAD group) and after training ( $n = 4$  each, 6-mo-old WT or 5xFAD Training group;  $n = 6$  each, 7-mo-old WT or 5xFAD Training group). Data are presented as mean  $\pm$  SEM.  $**P < 0.01$ ;  $***P < 0.001$ ; two-way ANOVA with Bonferroni's multiple comparisons test (A–E).

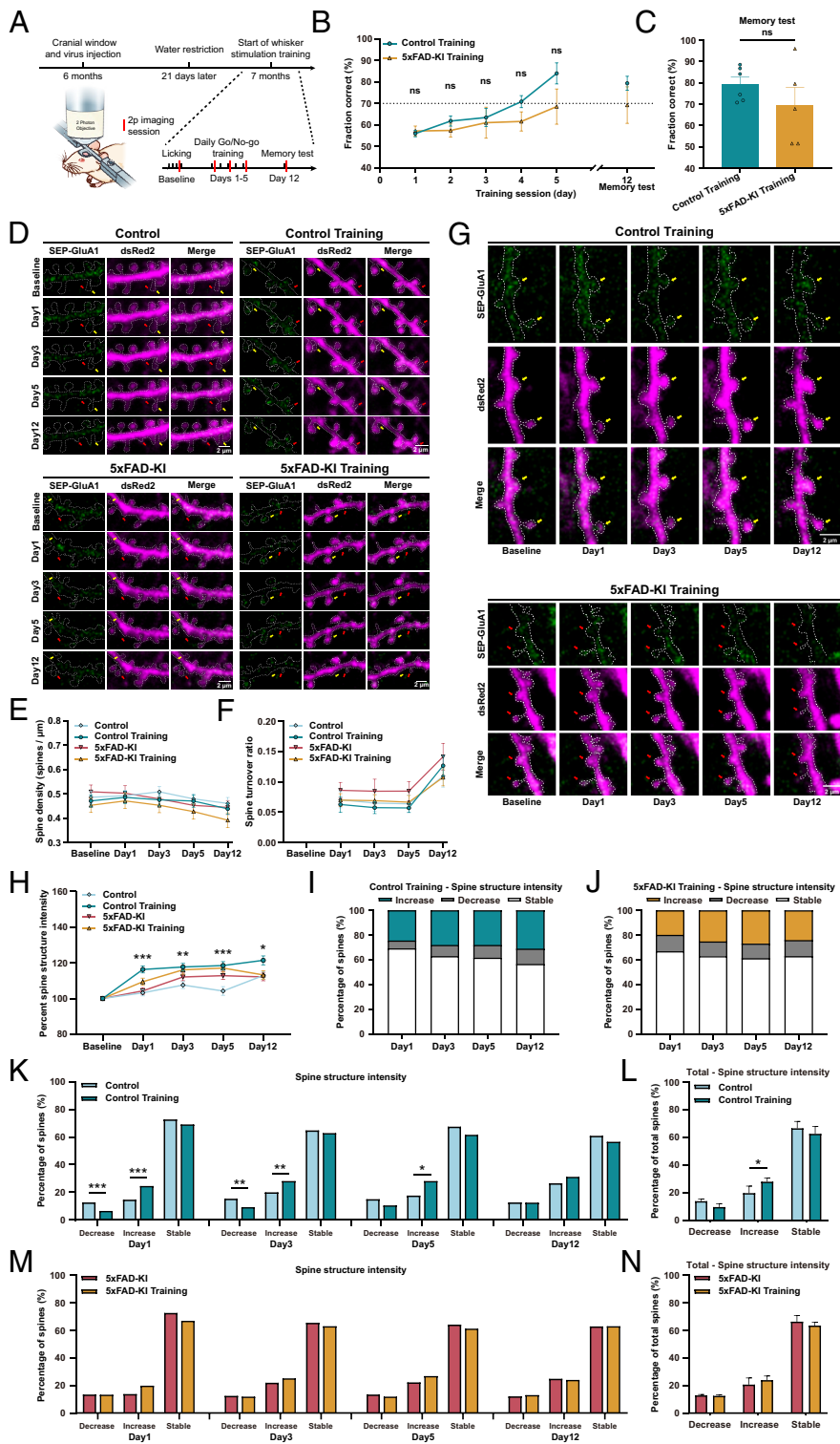


**Fig. 3.** Whisker stimulation-associated learning induces an increase in spine size in control but not 5x FAD-KI Mice. (A) Experimental timeline with schematic drawing of in vivo two-photon imaging. (B) Learning curves of 7-mo-old mice in the Go/No-go paradigm.  $n = 6$  (Control Training group),  $n = 5$  (5x FAD-KI Training group). (C) Behavioral performance of 7-mo-old mice at memory test.  $n = 6$  (Control Training group),  $n = 5$  (5x FAD-KI Training group). (D) Representative images of spines on layer 2/3 apical dendrites in the barrel cortex of Control or 5x FAD-KI mice over the course of Go/No-go training. Red arrows indicate spines added; yellow arrows indicate spines subtracted. Images are single-plane median-filtered images that were upscaled and contrast enhanced. (E and F) Spine density and spine turnover for dendrites imaged in different groups of mice (Control Training group:  $n = 22$  dendrites, five mice; Control Training group:  $n = 16$  dendrites, five mice; 5x FAD-KI Training group:  $n = 19$  dendrites, five mice; 5x FAD-KI group:  $n = 17$  dendrites, four mice). (G) Representative images of spines on layer 2/3 apical dendrites of Control or 5x FAD-KI Training mice over the course of Go/No-go training. Yellow and red arrows indicate the same spines across all imaging sessions. Images are single-plane median-filtered images that were upscaled and contrast enhanced. (H) Average spine structure intensity normalized to baseline over the course of Go/No-go training.  $*P < 0.05$ ,  $**P < 0.01$ ,  $***P < 0.001$ , Control Training mice versus Control mice. (I–N) The percentages of spines showing increase, decrease, or being stable in spine structure intensity during the course of learning in different groups of mice. Data are presented as a 100% stacked column chart in panels I, J, K, and M. (H–N) 396 spines and 23 dendrites in five Control Training mice; 302 spines and 16 dendrites in five Control mice; 354 spines and 19 dendrites in five 5x FAD-KI Training mice; 305 spines and 17 dendrites in four 5x FAD-KI mice. Data are presented as mean  $\pm$  SEM. ns, not significant;  $*P < 0.05$ ;  $**P < 0.01$ ;  $***P < 0.001$ ; two-way ANOVA with Bonferroni's multiple comparisons test (B, E, and F); unpaired two-tailed  $t$  test (C); two-way ANOVA with Bonferroni's multiple comparisons test (H); chi-square test with Bonferroni correction (K–N).

(Fig. 3D), and found no differences in dendritic spine density, percent added spine, percent subtracted spine, percent transient spine, or spine turnover ratio between 5xFAD-KI and Control mice during and after training (Fig. 3D–F and *SI Appendix*, Fig. S2G–I). While there was a significant increase in spine structure intensity (spine size) in Control mice during training, which was absent in 5xFAD-KI mice (Fig. 3G and H).

Next, we took advantage of the spatiotemporal resolution offered by *in vivo* imaging to look at changes/diversity in individual spines and found that individual spine size was quite dynamic across all four groups of mice (*SI Appendix*, Fig. S3A and B). Spines were classified into increase, decrease, and stable categories based on their average change in spine size during learning (Fig. 3I and J and *SI Appendix*, Fig. S3C). The proportion of spines in the increase category went up significantly in Control mice after training on day 1, day 3, and day 5, while the proportion of spines in the decrease category went down significantly on day 1 and day 3 (Fig. 3K and L and *SI Appendix*, Fig. S3D). However, no significant changes were detected in 5xFAD-KI mice (Fig. 3M and N and *SI Appendix*, Fig. S3E). These results indicate that the absence of spine size increase correlates with the learning deficits in 5xFAD mice in Go/No-go training.

**Dynamic Changes of Spine Surface AMPA Receptors Were Impaired in 5xFAD-KI Mice during Learning.** Next, we investigated the changes of AMPA receptor subunit GluA1 in Go/No-go paradigm via quantifying spine surface fluorescence intensity (*Materials and Methods*). There was a significant increase in spine surface GluA1 in Control mice during learning, while this increase was absent in 5xFAD-KI mice (Fig. 4A and B). Next, we took a look at the diversity of AMPA receptor dynamics in individual spines and found that the distribution of spine sGluA1 changes was significantly shifted toward larger increases after training in Control mice, while no such changes were detected in 5xFAD-KI mice (Fig. 4C–H). Spines were again classified into three categories: increase, decrease, and stable (Fig. 4I and J and *SI Appendix*, Fig. S4A). We found a larger fraction of spines with increasing GluA1 levels as well as a smaller fraction of spines with decreasing GluA1 levels in Control mice after training, while no such changes were apparent in 5xFAD-KI mice (Fig. 4K–N and *SI Appendix*, Fig. S4B and C). We noticed that the increase in spine surface GluA1 was obvious one day after training due to a bigger fraction of spines in increase category in Control mice; interestingly, there was also a fraction of spines showing increase in surface GluA1 in 5xFAD-KI mice one day after training, while the learning outcome was very different between these two groups. To further understand the role of this small fraction of spines in the increase category during learning, we compared spine sGluA1 changes in the increase category on the first training session (day 1) with late training sessions (day 3, day 5, and day 12) and found a strong positive correlation in Control mice (Fig. 4O and *SI Appendix*, Fig. S4D and E), while no such correlation was found in 5xFAD-KI mice (Fig. 4P and *SI Appendix*, Fig. S4F and G). Consistent with previous findings in motor cortex (24), our results show sensory-associated learning leads to an increase in spine surface GluA1 in Control mice, while this increase was absent in 5xFAD-KI mice. Furthermore, the stable increases in sGluA1 in a specific small fraction of spines (the increase category) in Control mice correlate with the learning performance, while no such fraction of spines was detected in 5xFAD-KI mice.

Next, we investigated the correlation between changes in spine size and spine surface GluA1 during Go/No-go training and found a positive correlation between changes in spine surface GluA1 and

changes in spine size in each of the imaging sessions in both Control and 5xFAD-KI mice (*SI Appendix*, Fig. S5A–D), which indicates that the correlation between spine sGluA1 and spine size is not altered in 5xFAD mice. In addition to spine surface GluA1 levels, we also analyzed surface GluA1 levels on the dendritic shaft adjacent to the spines (*SI Appendix*, Fig. S6A). There were no differences in shaft surface GluA1 levels on day 1, day 3, and day 5, other than a slight but statistically significant increase on day 12 (memory test) in Control mice after training; similarly, no shaft surface GluA1 level changes were detected in 5xFAD-KI mice (*SI Appendix*, Fig. S6A–M). These results suggest shaft sGluA1 dynamics is not altered in 5xFAD mice.

**Overactivation of Astrocytes and Microglia Corresponds to the Onset of Learning Deficits in 7-mo-old 5xFAD Mice.** Western blot results showed that training-induced changes of synaptosomal GluA1, GluN2A, and GluN2B levels in WT mice were absent in 7-mo-old 5xFAD mice (Fig. 2A and B). In addition, two-photon imaging results demonstrated that spine sGluA1 was significantly increased in 7-mo-old Control mice during learning, while no such changes were detected in 7-mo-old 5xFAD-KI mice (Fig. 4A and B). To explore the mechanisms underlying the abnormal changes of AMPA receptors in 5xFAD mice, we first investigated the distribution of A $\beta$  plaques in the S1BF in these four groups of mice (Fig. 5A). As expected, there was an increase in the number and area of A $\beta$  plaques in 6-mo-old 5xFAD mice compared to WT, and there were significantly more A $\beta$  plaques in 7-mo-old 5xFAD mice compared to 6-mo-old 5xFAD mice (Fig. 5B). Previous studies have shown that A $\beta$  plaque deposits could affect spine density within a 50- $\mu$ m radius of the plaque (39), we next explored whether A $\beta$  plaques would also lead to changes in AMPA receptors in mouse brain slices using immunofluorescence staining (Fig. 5C and *Materials and Methods*). Notably, there were no significant differences in the average GluA1 fluorescence intensity within a 50- $\mu$ m radius of A $\beta$  plaques between 6-mo-old 5xFAD mice and WT mice, while the average GluA1 fluorescence intensity surrounding A $\beta$  plaques was significantly reduced in 7-mo-old 5xFAD mice (Fig. 5D).

Mature astrocytes are involved in multiple processes in the central nervous system, such as neurotransmitter recycling, synapse formation, and synaptic plasticity (40–44). Excessive release of  $\gamma$ -aminobutyric acid (GABA) and adenosine triphosphate (ATP) by active astrocytes is related to AD pathogenesis, and activation of microglia has been observed in neurodegeneration, which could lead to the production of a large number of neuroimmune inflammatory factors (45–47). Microglia-associated inflammasomes have also been found to contribute to A $\beta$  clearance and synaptic pruning and remodeling (48–50). Thus, we took a look at the status of astrocytes and microglia in these groups and found that the area coverage of activated astrocytes and IBA1+ microglia in S1BF were significantly increased in 7-mo-old 5xFAD mice compared to 6-mo-old 5xFAD mice, while no such differences were observed between 6-mo-old 5xFAD mice and WT mice (Fig. 5E–G). Similarly, there was significantly more IBA1+ microglia in 7-mo-old 5xFAD mice compared to 6-mo-old 5xFAD mice (Fig. 5H). We also observed a significant increase in the number of IBA1+ microglia surrounding A $\beta$  plaques and colocalization with A $\beta$  plaques in 7-mo-old 5xFAD mice compared to 6-mo-old 5xFAD mice (Fig. 5I–K). Additionally, there was a notable increase in the percentage of the total imaging field covered by colocalized plaque and IBA1 staining in 7-mo-old 5xFAD mice compared to 6-mo-old 5xFAD mice (Fig. 5L). At the same time, the percentage of activated microglia (deramified microglia, hypertrophy of the cell body, and shortened processes) increased

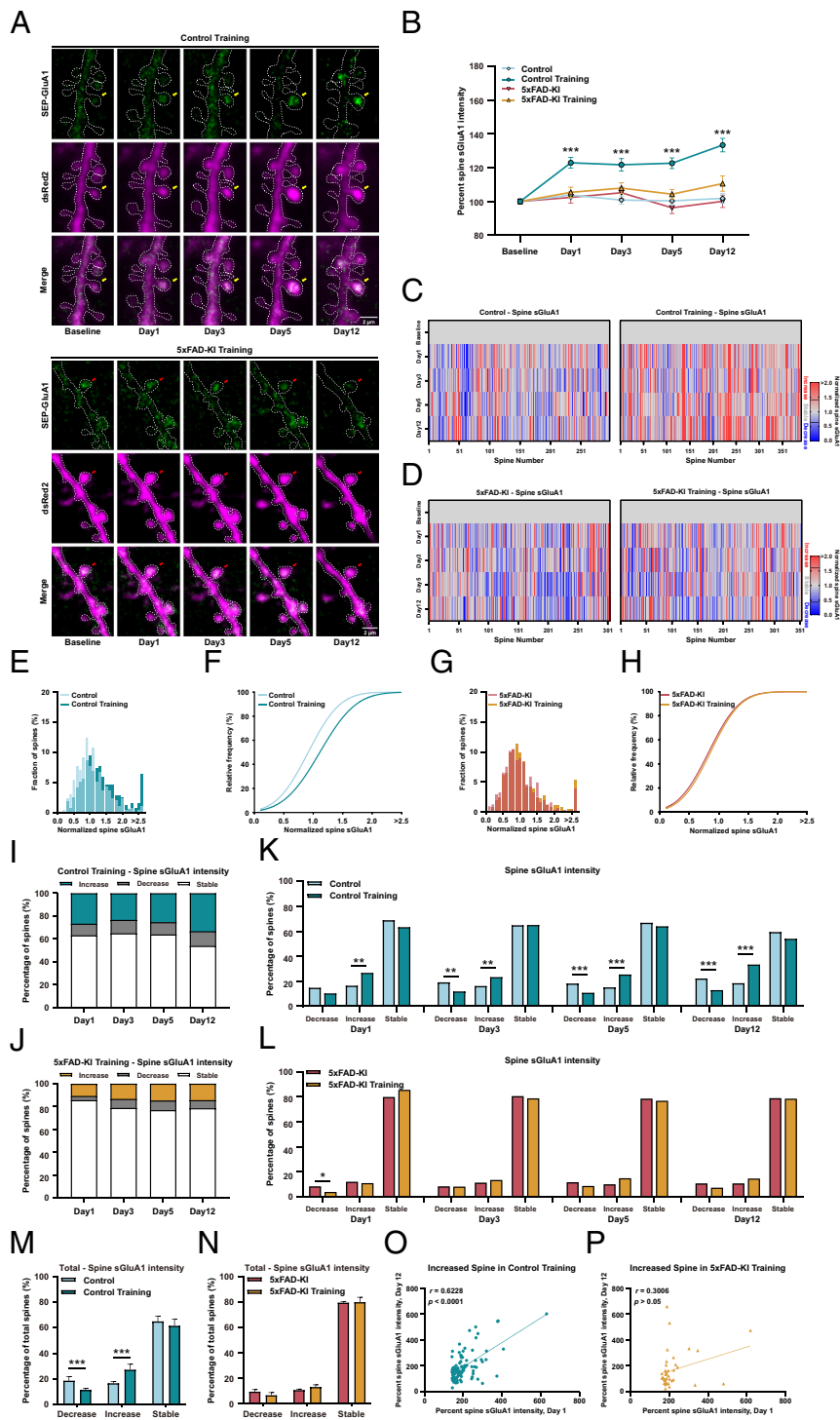


**Fig. 4.** Dynamic changes of spine surface AMPA receptors were impaired in 5xFAD-KI mice during learning. (A) Representative images of spines on layer 2/3 apical dendrites in the barrel cortex of Control and 5xFAD-KI mice over the course of Go/No-go training. Yellow and red arrows indicate the same spines across all imaging sessions. Images are single-plane median-filtered images that were upscaled and contrast enhanced. (B) Average spine surface GluA1 intensity normalized to baseline over the course of Go/No-go training.  $***P < 0.001$ , Control Training mice versus Control mice. (C and D) Heatmap showing amount of spine surface GluA1 in individual spines of different groups of mice. Each column represents a single spine. The surface GluA1 level of each spine is normalized to its baseline and columns are sorted by average surface GluA1 change during training. (E) Distribution histogram of average spine surface GluA1 change in Control Training and Control mice. (F) Cumulative distribution of average spine surface GluA1 change in Control Training and Control mice. (G) Distribution histogram of average spine surface GluA1 change in 5xFAD-KI Training and 5xFAD-KI mice. (H) Cumulative distribution of average spine surface GluA1 change in 5xFAD-KI Training and 5xFAD-KI mice. (I–N) Percentages of spines showing increase, decrease, or being stable in spine surface GluA1 intensity at different time points in different groups of mice. Data are presented as a 100% stacked column chart in panels I–L. (B–N) 391 spines and 23 dendrites in five Control Training mice; 298 spines and 16 dendrites in five Control mice; 354 spines and 19 dendrites in five 5xFAD-KI Training mice; 304 spines and 17 dendrites in four 5xFAD-KI mice. (O) Comparison of spine surface GluA1 change in spines showing increase on the first training session (day 1) with late training session (day 12) in Control mice with linear fits ( $r = 0.6228$ ,  $P < 0.0001$ ). In addition, 104 spines and 23 dendrites in five Control Training mice;  $r$ , Pearson's linear correlation coefficient;  $p$ , Pearson's correlation. (P) Comparison of spine surface GluA1 change in spines showing increase on the first training session (day 1) with late training session (day 12) in 5xFAD-KI mice with linear fits ( $r = 0.3006$ ,  $P = 0.0667$ ). Thirty-eight spines and 19 dendrites in five 5xFAD-KI Training mice;  $r$ , Pearson's linear correlation coefficient;  $p$ , Pearson's correlation. Data are presented as mean  $\pm$  SEM. ns, not significant;  $*P < 0.05$ ;  $**P < 0.01$ ;  $***P < 0.001$ ; two-way ANOVA with Bonferroni's multiple comparisons test (B); two-sample Kolmogorov–Smirnov test (F and H); chi-square test with Bonferroni correction (K–N).

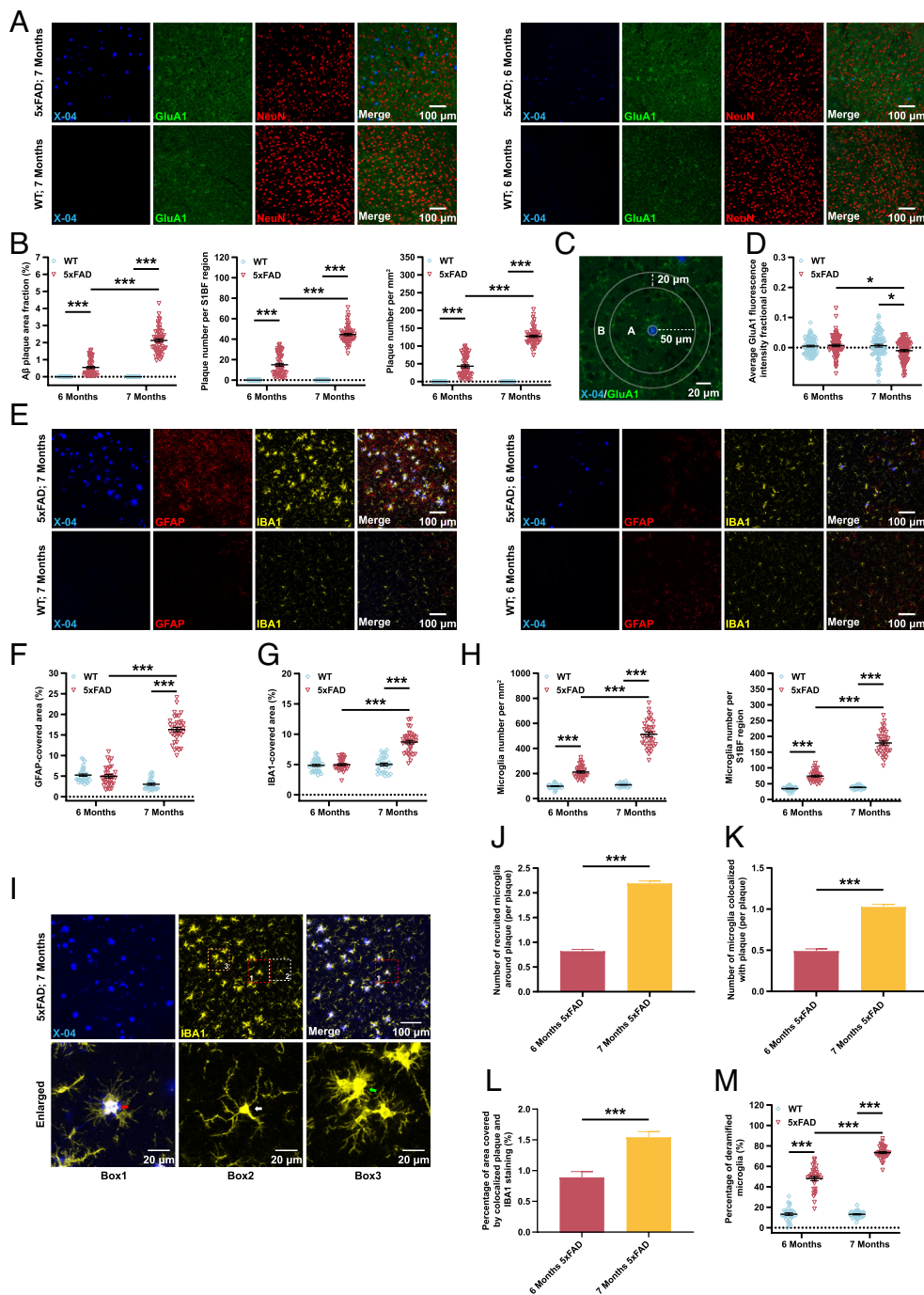


**Fig. 5.** Overactivation of astrocytes and microglia corresponds to the onset of learning deficits in 7-mo-old 5xFAD mice. (A) Representative immunofluorescence images of A $\beta$  (Methoxy-X04, X-04, blue), GluA1 (green), and NeuN (red) in the S1BF of different groups of mice. Bar, 100  $\mu$ m. (B) Quantitative analysis of A $\beta$  staining from A. (C) Schematic illustration of A $\beta$  amyloid plaques. (D) Fractional changes of the average GluA1 fluorescence intensity in the vicinity (<50  $\mu$ m) of A $\beta$  amyloid plaques. (E) Representative immunofluorescence images of A $\beta$  (X-04, blue), GFAP (red), and IBA1 (yellow) in the S1BF of different groups of mice. Bar, 100  $\mu$ m. (F) Quantitative analysis of the covered area of astrocytes in the S1BF from E. (G and H) Quantitative analysis of the covered area and number of IBA1+ microglia in the S1BF from E. (I) Representative immunofluorescence images of A $\beta$  (X-04, blue) and IBA1 (yellow) in the S1BF of 7-mo-old mice. Red arrow in box1 enlarged image indicates the colocalization of microglia with A $\beta$  plaques. Representative immunofluorescence images of ramified (white arrow in box2 enlarged) or deramified (green arrow in box3 enlarged) IBA1 positive microglia. Top, bar, 100  $\mu$ m; bottom, bar, 20  $\mu$ m. (J) Quantitative analysis of the number of IBA1+ microglia around A $\beta$  plaques in the S1BF of 6- and 7-mo-old 5xFAD mice from I. 672 plaques in three 6-mo-old 5xFAD mice; 2,038 plaques in three 7-mo-old 5xFAD mice. (K) Quantitative analysis of the number of microglia colocalized with plaque in the S1BF of 6- and 7-mo-old 5xFAD mice from I. 672 plaques in three 6-mo-old 5xFAD mice; 2,038 plaques in three 7-mo-old 5xFAD mice. (L) Quantitative analysis of the percentage of the total imaging field covered by colocalized plaque and IBA1 staining in the S1BF of 6- and 7-mo-old 5xFAD mice from I. Thirty-two imaging fields in three 6-mo-old 5xFAD mice; 37 imaging fields in three 7-mo-old 5xFAD mice. (M) Quantitative analysis of the percentage of deramified IBA1+ microglia in the S1BF from I. Data are presented as mean  $\pm$  SEM. \* $P$  < 0.05; \*\* $P$  < 0.01; \*\*\* $P$  < 0.001;  $n$  = 3 per group. Two-way ANOVA with Bonferroni's multiple comparisons test (B, D, F–H, and M); Mann–Whitney  $U$  test (J–L).

significantly in 7-mo-old 5xFAD mice compared to 6-mo-old 5xFAD mice (Fig. 5M). These findings indicate that overactivation of astrocytes and microglia corresponds to the onset of learning

deficits in 7-mo-old 5xFAD mice. Although whether the differences of GluA1 changes surrounding A $\beta$  plaques are mainly due to overactivation of microglia and astrocytes remains unclear, these



differences very likely play an important role in the learning deficits in 7-mo-old 5xFAD mice.

## Discussion

In our study, utilizing the SEP-GluA1 knockin line, we investigated endogenous AMPA receptor dynamics in real time in 5xFAD mice. We found that there were learning deficits in 7-mo-old 5xFAD mice in a whisker-associated Go/No-go paradigm but not in 6-mo-old 5xFAD mice (Fig. 1 *H* and *I*). Significant increases were detected in the synaptosomal protein levels of GluA1, GluA2, GluN2A, and GluN2B in WT mice after training, while no such changes were detected in 7-mo-old 5xFAD mice (Fig. 2 *A* and *B*). AMPA receptor dynamics in individual spines were monitored via two-photon imaging, and there was a significant increase in spine sGluA1 levels in Control mice during training, but not in 5xFAD-KI mice (Fig. 4 *A* and *B*). In addition, there was a significant increase in astrocytes and microglia activation in the S1BF in 7-mo-old 5xFAD mice compared to 6-mo-old 5xFAD mice (Fig. 5 *F–M*). These findings suggest that abnormal spine surface GluA1 dynamics, which could be partially caused by astrocytes and microglia overactivation, correlates well with learning deficits in 7-mo-old 5xFAD mice.

There were significant increases in the protein levels of GluA1 and GluA2 in WT mice after whisker-associated learning, while no changes were detected in 7-mo-old 5xFAD mice (Fig. 2 *A* and *B*). Our results are consistent with previous findings in motor cortex that spine surface GluA1 levels increased during motor learning and correlated well with task performance. Our results show that training-induced increase in synaptosomal GluA2 is absent in both 6-mo-old and 7-mo-old 5xFAD mice, and it is known that AMPA receptors are tetrameric complex composed of four subunits, GluA1, GluA2, GluA3, and GluA4. GluA1 and GluA4 have long tails, while GluA2 and GluA3 have relatively short tails, long-tailed and short-tailed AMPARs show different trafficking patterns (1, 6, 7). GluA1/GluA2, GluA2/GluA3 subtypes are the major types of AMPARs in the cerebral cortex and hippocampus, even though only accounts for a small fraction, GluA1/GluA1 subtype still plays an important role in cognitive function due to its calcium permeability (1, 3, 6, 7, 51). Previous studies have shown that trafficking of GluA1/GluA2 type of AMPA receptors is neuronal activity dependent, while trafficking of GluA2/GluA3 subtype of AMPA receptors is nonactivity dependent. In addition, studies have shown that GluA1 is more selective for synaptic plasticity while GluA2 is more selective for homeostatic plasticity (6, 52). We suspect that both GluA1 and GluA2 are contributing to learning deficits in AD animals, in other words, both synaptic plasticity and homeostatic plasticity might be impaired. Overall, GluA1 and GluA2 posttranslational modifications and/or binding partners can regulate distinct forms of plasticity, and it is reasonable to speculate that plasticity predominantly regulated by GluA1 may be more important for the learning task in our study.

In addition, we also assessed the changes in synaptosomal GluA3 protein levels. There were no significant differences in the homogenous GluA3 level between 5xFAD and WT groups both at the age of 6 and 7 mo. Similarly, synaptosomal GluA3 level between 6-mo-old 5xFAD and WT groups was not significantly different. Surprisingly, there was an increase in synaptosomal GluA3 protein level in 7-mo-old 5xFAD mice after training (*SI Appendix, Fig. S7B*). We speculate that this could be due to defects in AMPA receptor equilibrium or subunits switch in 5xFAD mice. It will be interesting to further investigate the role of AMPA receptor subunits switch, or the lack thereof in AD models, during learning.

AMPA receptors mediate the majority of fast excitatory synaptic transmission in the central nervous system. Previous *in vivo* studies have provided and will continue to provide valuable insights in the molecular mechanisms underlying synaptic plasticity in animal behavior (22–26, 53–55), but these methods used exogenous overexpression of SEP-tagged AMPARs which could result in protein mistargeting. The SEP-GluA1 knockin mice generated by the Hugarir group have enabled tracking of endogenous AMPAR dynamics in awake-behaving animals. It has been well known that AD animal models have learning deficits; however, whether or how endogenous AMPA receptors change in AD models has not been investigated. In this study, we employed 5xFAD-KI mice and monitored endogenous AMPA receptor dynamics during a whisker-associated Go/No-go learning paradigm. Our results showed that Go/No-go training induced an increase in endogenous spine surface GluA1 level over the course of learning in the barrel cortex of Control mice (Fig. 4 *A* and *B*), which is consistent with previous findings with overexpressed SEP-GluA1 in motor learning. However, Go/No-go training did not result in dramatic changes in shaft surface GluA1 level (*SI Appendix, Fig. S6A*), which is different from previous findings that an increase was detected in shaft surface GluA1 level after acute whisker deflection or motor learning. This discrepancy in shaft surface GluA1 could result from overexpressed versus endogenous SEP-GluA1, it could also be due to the different property of barrel cortex versus motor cortex, or acute deflection versus whisker-associated learning. In any case, it would be interesting to further decipher AMPA receptor dynamics during learning and memory at brain-wide scale by utilizing this SEP-GluA1 knockin line in both health and disease conditions.

The observation of dynamic changes in synaptic strength after learning is consistent with the Hebbian theory of activity-dependent synaptic plasticity to strengthen task-relevant neuronal circuits. At the level of individual spines, the frequency distribution of spine sGluA1 changes was significantly shifted to the right in Control mice after training (Fig. 4 *E* and *F*), and a larger fraction (~27%) of the spines showed increased surface GluA1 (Fig. 4*M*). A fraction of spines also showed increases in spine sGluA1 in 5xFAD-KI mice; however, there was a significant positive correlation in the fraction of spines with increased surface GluA1 among day 1, day 3, day 5, and day 12 in Control mice (Fig. 4*O* and *SI Appendix, Fig. S4 D and E*), while no such correlation was detected in 5xFAD-KI mice with learning deficits (Fig. 4*P* and *SI Appendix, Fig. S4 F and G*). Our results also indicated that stable increase in spine surface GluA1 correlated well with whisker-associated learning, while no such correlation was found in 5xFAD-KI mice; in the meantime, no differences were detected in spine turnover/dynamics between these two groups of mice, which indicates that the absence of a correlated increase in spine surface GluA1 in a small fraction of spines plays an important role in learning deficits in AD animals. These results suggest that AMPA receptor plasticity and structural plasticity (via spine size changes) play complementary roles during learning, with correlated changes in a small fraction of stable spines being more relevant, at least in this whisker-associated learning paradigm, which is consistent with previous findings that new born spines that stayed stable might be more relevant to learning than transient spines (56).

Although there were statistically more A $\beta$  plaques deposits in 7-mo-old 5xFAD mice compared to 6-mo-old 5xFAD mice (Fig. 5*B*), both were significantly more than WT animals, and it was extremely puzzling when we first observed that 7-mo-old 5xFAD mice showed learning deficits but 6-mo-old 5xFAD mice did not. Next, we turned our focuses onto neuroinflammation and

found that there were much more astrocytes and microglia activation in 7-mo-old 5xFAD mice, which could lead to the decreases in AMPA receptor distribution surrounding A $\beta$  plaques and subsequently learning deficits (Fig. 5 C–H). It has been shown that A $\beta$  plaques can drive endocytosis of synaptic AMPA receptors and lead to loss of surface AMPA and NMDA receptors (57). AMPA receptors play an essential role in A $\beta$ -induced disruption of synaptic structure and function; synaptic removal of AMPA receptors is necessary and sufficient to produce loss of dendritic spines. Previous studies have shown that synapse loss in AD correlates with cognitive decline (58). Due to neuroinflammation, microglia activation could mediate synaptic loss in AD, which is related to age and/or stage of the disease. A $\beta$  plaque deposition shows toxic effects on synapses and hippocampal LTP. Activated microglia and astrocytes could engulf synaptic material exposed to A $\beta$  plaques, excessive pruning or engulfment of synapses might mediate the decrease of AMPA receptor levels in the vicinity of A $\beta$  plaques. Neuroinflammation defects have been documented in AD patients and animal models (59, 60); our results further suggest neuroinflammation-related changes, especially neuroinflammation-related AMPA receptor changes would be an interesting direction to better understand AD pathology.

In conclusion, monitoring the dynamic changes of AMPA receptors *in vivo* provides valuable insight to better understand learning and memory. Our study achieves direct observation of endogenous AMPA receptor dynamics *in vivo* in AD animal models during learning. Our findings have advanced our understanding of synaptic basis for the learning deficits in 5xFAD mice and paved the way for studying endogenous AMPA receptor dynamics in disease animal models.

## Materials and Methods

**Animals.** All animal experimental procedures and studies were approved by the animal care and use committee of the animal facility at Peking University Health Science Center.

The SEP-GluA1 KI mice (C57BL/6J) were a gift from Richard Huganir's lab at the Johns Hopkins University School of Medicine (Baltimore, USA). The 5xFAD mice (B6SJL) (MMRRC Strain #034840-JAX) were a gift from Chen Zhang's lab at Capital Medical University (Beijing, China). The SEP-GluA1 KI mice (B6SJL) were generated by crossing SEP-GluA1 KI mice (C57BL/6J) with WT mice (SJL). Six- or 7-mo-old male 5xFAD mice (B6SJL) were used for early Go/No-go paradigm exploration, western blot, and immunostaining. 5xFAD mice (B6SJL) and SEP-GluA1 KI mice (B6SJL) were crossed to generate 5xFAD SEP-GluA1 KI (Het); 5xFAD SEP-GluA1 KI (Het) were crossed with SEP-GluA1 KI mice (B6SJL) to generate 5xFAD SEP-GluA1 KI (Hom) and SEP-GluA1 KI (Hom). 5xFAD SEP-GluA1 KI (Hom) (named as 5xFAD-KI) and SEP-GluA1 KI (Hom) (named as Control) mice were used for two-photon imaging and Go/No-go training.

**Go/No-go Paradigm.** Mice were anesthetized with 1.25% Avertin (0.2 mL/10 g) intraperitoneal (i.p.) injection and implanted with a head plate to the skull using dental cement (C&B Metabond, Parkell). Mice were given at least 1 wk to recover from surgery before water restriction. The Go/No-go procedure was adopted and modified from a previous study (61). There was 7 to 10 d of water restriction period before start of training. Training began with three or four daily sessions (~10 min for each mouse), during which mice were rewarded with a drop of water for licking the lickport with no stimulation or task. Mice were then trained daily with whisker stimulation. In Go/No-go paradigm, the deflection pole was placed near the C2 whisker. With a large amplitude stimulus (Go trail), almost all the whiskers on the stimulated side of the mouse would be deflected, whereas with a small amplitude stimulus (No-go trail), only C2 or a few whiskers would be deflected. The sequence of each trial was as follows (Fig. 1B). The type of trial (Go or No-go) was chosen randomly, while no more than three consecutive trials of the same type. To minimize the possible auditory cues caused by the movement of the pole, white noise was played simultaneously during Go/No-go training. Mice had a 2-s window from the

start of the pole stimulation to either lick ("Go" response) or withhold a lick ("No-go" response). Lick was only counted as a response if mice licked in the "response period." Correct No-go response (correct rejection) was not rewarded, and incorrect Go response (miss) was not punished. Correct Go response (hit) was rewarded with a drop of water (~6  $\mu$ L). An incorrect No-go response ("false alarm") triggered a "timeout" period in which the trial was paused for 3 s. If the mouse licked during this timeout, the timeout period would restart. If a mouse stopped making any response for at least 10 trials in a training session, these trials were excluded from the analysis. Mice performance (fraction correct) was assessed by the sum of hits and correct rejection trials divided by total number of trials. The formula used is as follows.

$$\text{Fraction Correct (100\%)} = \frac{\# \text{ Hits} + \# \text{ Correct rejection}}{\# \text{ Trials}}$$

The Go/No-go task is a widely used training task for assessing function of somatosensory cortex (61–63). The definition of "expert level" utilizes the same formula but the value varies between 65 to 80%, based on the WT mice cohort and the learning curve, we choose 70% as the cut-off threshold for expert. Mice were considered experts when performance reached  $\geq 70\%$  correct for two consecutive days and training would be stopped. Memory tests were performed a week after the last training session.

**Craniotomy and Virus Injection.** Viruses used in our study were ordered from BrainCase Technology: AAV2/9-CaMKII- $\alpha$ -CCSP-dsRed2-2E4 [ $5.28 \times 10^{12}$  viral genomes per mL (V.G./mL)]. Control and 5xFAD-KI mice were anesthetized with Avertin and implanted with a  $3 \times 3$ -mm cranial window over the barrel cortex region at the age of 6 mo as previously described (26). Viruses were injected (100 nL per site, 2 to 3 sites per animal; depth ~300  $\mu$ m) into the barrel cortex as previously described (64). After injection, the window and skull were sealed with dental cement (C&B Metabond, Parkell). A custom-made metal head plate was attached to the skull to fix the mice for Go/No-go and two-photon imaging. The antibiotics trimethoprim and sulfamethoxazole were chronically administered in the drinking water. Mice were housed individually after surgery and allowed to recover and virus expression for 3 to 4 wk before Go/No-go training and imaging.

**Optical Intrinsic Signal Imaging.** Optical intrinsic signal imaging was performed 2 to 3 wk after the cranial window surgery as described previously (26, 65). Mice were anesthetized and maintained with 0.5% isoflurane on a heating pad supplemented by xylazine (13 mg/kg).

**Two-Photon Imaging.** After the completion of the Go/No-go training, Control and 5xFAD-KI mice were taken for two-photon imaging of the S1BF region within 2 h after training. SEP-GluA1 and dsRed2 were excited at 910 nm with 10 to 100 mW of power delivered to the back-aperture of the objective. Green and red fluorescence signals were separated by dichroic mirrors and filters (ET525/50m for the green channel, ET605/70m for the red channel). To exclude the possibility of any cross-channel signal bleed-through from the red (dsRed2) channel into the green (SEP-GluA1) channel, we imaged animals expressing SEP-GluA1 only or expressing dsRed2 only under the same imaging setting, as shown in *SI Appendix, Fig. S2 E and F*, no signals in the green channel were detected in animals expressing only dsRed2, and no signals in the red channel were detected in animals expressing SEP-GluA1 only, which demonstrates that no bleed through between red and green channels under our imaging conditions. Representative images shown in the figures were median or GaussianBlur-filtered and contrast enhanced.

**Analysis of In Vivo Two-Photon Imaging Data.** The same dendritic tracing and spine labeling were used to analyze both spine turnover and intensity. Spines were classified into increase, decrease, or stable categories based on their average change in spine size/sGluA1 levels compared to baseline. The threshold for these categories was set based on the variability in nontrained control mice and was defined at baseline  $\pm$  one SD. Spines increasing more than one SD during training were classified as increase, spines decreasing more than one SD were classified as decrease, and remaining spines were defined as stable.

**Statistical Analysis.** Unless otherwise stated, all data were presented as mean  $\pm$  SEM. Corresponding types of statistical tests used, n numbers, and statistical

significance were indicated in the figure legends. Statistical analysis was conducted with SPSS (Version 27) or GraphPad Prism (Version 9.0) software.

Additional methods are included in [SI Appendix](#).

**Data, Materials, and Software Availability.** All study data are included in the article and/or [supporting information](#).

**ACKNOWLEDGMENTS.** We thank Dr. Richard Huganir (Johns Hopkins University School of Medicine) for providing the SEP-GluA1 KI mice. We thank Dr. Eric Gouaux (Oregon Health & Science University) for providing anti-GluA1 antibody. We thank Dr. Robert H. Cudmore (UC Davis), Dr. Richard Roth (Stanford University) for their assistance with the Map Manager software. We thank Shuting Liu (School of Basic Medical Sciences, Peking University) for drawing the schematic diagram. We thank Dr. Zengcai Guo (Tsinghua University) for assistance in

whisker stimulation system setup. This work was supported by STI2030-Major Projects 2022ZD0204900 and the National Natural Science Foundation of China (Grants 31970911 and 81821092).

Author affiliations: <sup>a</sup>Neuroscience Research Institute and Department of Neurobiology, School of Basic Medical Sciences, Peking University, Key Laboratory for Neuroscience, Ministry of Education of China and National Health Commission of the People's Republic of China, Beijing 100083, China; <sup>b</sup>PKU-IDG/McGovern Institute for Brain Research, Beijing 100871, China; <sup>c</sup>Center of Medical and Health Analysis, Peking University Health Science Center, Beijing 100083, China; <sup>d</sup>Academy of Medical Engineering and Translational Medicine, Tianjin University, Tianjin 300072, China; <sup>e</sup>School of Basic Medical Sciences, Beijing Key Laboratory of Neural Regeneration and Repair, Advanced Innovation Center for Human Brain Protection, Capital Medical University, Beijing 100069, China; and <sup>f</sup>School of Psychological and Cognitive Sciences, Peking University, Beijing 100871, China

1. J. D. Shepherd, R. L. Huganir, The cell biology of synaptic plasticity: AMPA receptor trafficking. *Annu. Rev. Cell Dev. Biol.* **23**, 613–643 (2007).
2. S. B. Chidambaram *et al.*, Dendritic spines: Revisiting the physiological role. *Prog. Neuro-psychopharmacol. Biol. Psychiatry* **92**, 161–193 (2019).
3. I. Song, R. L. Huganir, Regulation of AMPA receptors during synaptic plasticity. *Trends Neurosci.* **25**, 578–588 (2002).
4. R. Malinow, R. C. Malenka, AMPA receptor trafficking and synaptic plasticity. *Annu. Rev. Neurosci.* **25**, 103–126 (2002).
5. V. A. Derkach, M. C. Oh, E. S. Guire, T. R. Soderling, Regulatory mechanisms of AMPA receptors in synaptic plasticity. *Nat. Rev. Neurosci.* **8**, 101–113 (2007).
6. G. H. Diering, R. L. Huganir, The AMPA receptor code of synaptic plasticity. *Neuron* **100**, 314–329 (2018).
7. R. L. Huganir, R. A. Nicoll, AMPARs and synaptic plasticity: The last 25 years. *Neuron* **80**, 704–717 (2013).
8. H. Hampel *et al.*, The future of Alzheimer's disease: The next 10 years. *Prog. Neurobiol.* **95**, 718–728 (2011).
9. L. Volk, S. L. Chiu, K. Sharma, R. L. Huganir, Glutamate synapses in human cognitive disorders. *Annu. Rev. Neurosci.* **38**, 127–149 (2015).
10. A. L. Guillozet, S. Weintraub, D. C. Mash, M. M. Mesulam, Neurofibrillary tangles, amyloid, and memory in aging and mild cognitive impairment. *Arch. Neurol.* **60**, 729–736 (2003).
11. E. Drummond, S. Nayak, G. Pires, B. Ueberheide, T. Wisniewski, Isolation of amyloid plaques and neurofibrillary tangles from archived Alzheimer's disease tissue using laser-capture microdissection for downstream proteomics. *Methods Mol. Biol.* **1723**, 319–334 (2018).
12. T. Arendt, M. K. Bruckner, M. Morawski, C. Jager, H. J. Gertz, Early neurone loss in Alzheimer's disease: Cortical or subcortical? *Acta Neuropathol. Commun.* **3**, 10 (2015).
13. P. D. Coleman, D. G. Flood, Neuron numbers and dendritic extent in normal aging and Alzheimer's disease. *Neurobiol. Aging* **8**, 521–545 (1987).
14. P. R. Hof, K. Cox, J. H. Morrison, Quantitative analysis of a vulnerable subset of pyramidal neurons in Alzheimer's disease: I. Superior frontal and inferior temporal cortex. *J. Comp. Neurol.* **301**, 44–54 (1990).
15. G. M. Shankar *et al.*, Amyloid-beta protein dimers isolated directly from Alzheimer's brains impair synaptic plasticity and memory. *Nat. Med.* **14**, 837–842 (2008).
16. D. M. Walsh, D. J. Selkoe, A beta oligomers—A decade of discovery. *J. Neurochem.* **101**, 1172–1184 (2007).
17. C. G. Almeida *et al.*, Beta-amyloid accumulation in APP mutant neurons reduces PSD-95 and GluR1 in synapses. *Neurobiol. Dis.* **20**, 187–198 (2005).
18. M. Sheng, B. L. Sabatini, T. C. Sudhof, Synapses and Alzheimer's disease. *Cold Spring Harb. Perspect. Biol.* **4**, a005777 (2012).
19. W. Yu, B. Lu, Synapses and dendritic spines as pathogenic targets in Alzheimer's disease. *Neural. Plast.* **2012**, 247150 (2012).
20. Y. Zhang, O. Guo, Y. Huo, G. Wang, H. Y. Man, Amyloid-beta induces AMPA receptor ubiquitination and degradation in primary neurons and human brains of Alzheimer's disease. *J. Alzheimers Dis.* **62**, 1789–1801 (2018).
21. W. Q. Zhao *et al.*, Inhibition of calcineurin-mediated endocytosis and alpha-amino-3-hydroxy-5-methyl-4-isoxazolepropionic acid (AMPA) receptors prevents amyloid beta oligomer-induced synaptic disruption. *J. Biol. Chem.* **285**, 7619–7632 (2010).
22. G. H. Diering *et al.*, Homer1a drives homeostatic scaling-down of excitatory synapses during sleep. *Science* **355**, 511–515 (2017).
23. H. Makino, R. Malinow, AMPA receptor incorporation into synapses during LTP: The role of lateral movement and exocytosis. *Neuron* **64**, 381–390 (2009).
24. R. H. Roth *et al.*, Cortical synaptic AMPA receptor plasticity during motor learning. *Neuron* **105**, 895–908.e5 (2020).
25. A. Suresh, A. Dunaevsky, Relationship between synaptic AMPAR and spine dynamics: Impairments in the FXS mouse. *Cereb. Cortex* **27**, 4244–4256 (2017).
26. Y. Zhang, R. H. Cudmore, D. T. Lin, D. J. Linden, R. L. Huganir, Visualization of NMDA receptor-dependent AMPA receptor synaptic plasticity in vivo. *Nat. Neurosci.* **18**, 402–407 (2015).
27. A. R. Graves *et al.*, Visualizing synaptic plasticity in vivo by large-scale imaging of endogenous AMPA receptors. *Life* **10**, 1–29 (2021).
28. F. Kosel, J. M. S. Pelley, T. B. Franklin, Behavioural and psychological symptoms of dementia in mouse models of Alzheimer's disease-related pathology. *Neurosci. Biobehav. Rev.* **112**, 634–647 (2020).
29. H. Oakley *et al.*, Intraneuronal beta-amyloid aggregates, neurodegeneration, and neuron loss in transgenic mice with five familial Alzheimer's disease mutations: Potential factors in amyloid plaque formation. *J. Neurosci.* **26**, 10129–10140 (2006).
30. N. A. Xiao *et al.*, Reduction of glucose metabolism in olfactory bulb is an earlier Alzheimer's disease-related biomarker in 5XFAD mice. *Chin. Med. J. (Engl)* **128**, 2220–2227 (2015).
31. S. D. Girard *et al.*, Evidence for early cognitive impairment related to frontal cortex in the 5XFAD mouse model of Alzheimer's disease. *J. Alzheimers Dis.* **33**, 781–796 (2013).
32. L. Devi, M. Ohno, Genetic reductions of beta-site amyloid precursor protein-cleaving enzyme 1 and amyloid-beta ameliorate impairment of conditioned taste aversion memory in 5XFAD Alzheimer's disease model mice. *Eur. J. Neurosci.* **31**, 110–118 (2010).
33. J. Hongpaisan, M. K. Sun, D. L. Alkon, PKC epsilon activation prevents synaptic loss, Abeta elevation, and cognitive deficits in Alzheimer's disease transgenic mice. *J. Neurosci.* **31**, 630–643 (2011).
34. T. J. Flanagan, Y. Xue, S. Kishan Rao, A. Dhanushkodi, M. P. McDonald, Abnormal vibrissa-related behavior and loss of barrel field inhibitory neurons in 5xFAD transgenics. *Genes. Brain Behav.* **13**, 488–500 (2014).
35. G. Yang, F. Pan, W. B. Gan, Stably maintained dendritic spines are associated with lifelong memories. *Nature* **462**, 920–924 (2009).
36. K. P. Berry, E. Nedivi, Spine dynamics: Are they all the same? *Neuron* **96**, 43–55 (2017).
37. Y. Zuo, G. Yang, E. Kwon, W. B. Gan, Long-term sensory deprivation prevents dendritic spine loss in primary somatosensory cortex. *Nature* **436**, 261–265 (2005).
38. D. H. Bhatt, S. Zhang, W. B. Gan, Dendritic spine dynamics. *Annu. Rev. Physiol.* **71**, 261–282 (2009).
39. T. Bittner *et al.*, Amyloid plaque formation precedes dendritic spine loss. *Acta Neuropathol.* **124**, 797–807 (2012).
40. A. J. Barker, E. M. Ullian, Astrocytes and synaptic plasticity. *Neuroscientist* **16**, 40–50 (2010).
41. N. J. Allen, Astrocyte regulation of synaptic behavior. *Annu. Rev. Cell Dev. Biol.* **30**, 439–463 (2014).
42. W. S. Chung, N. J. Allen, C. Eroglu, Astrocytes control synapse formation, function, and elimination. *Cold Spring Harb. Perspect. Biol.* **7**, a020370 (2015).
43. P. G. Haydon, G. Carmignoto, Astrocyte control of synaptic transmission and neurovascular coupling. *Physiol. Rev.* **86**, 1009–1031 (2006).
44. M. Oksanen *et al.*, Astrocyte alterations in neurodegenerative pathologies and their modeling in human induced pluripotent stem cell platforms. *Cell Mol. Life Sci.* **76**, 2739–2760 (2019).
45. S. Bachiller *et al.*, Microglia in neurological diseases: A road map to brain-disease dependent-inflammatory response. *Front. Cell Neurosci.* **12**, 488 (2018).
46. S. Hickman, S. Izzy, P. Sen, L. Morsett, J. El Khoury, Microglia in neurodegeneration. *Nat. Neurosci.* **21**, 1359–1369 (2018).
47. M. Sochocka, B. S. Diniz, J. Leszek, Inflammatory response in the CNS: Friend or foe? *Mol. Neurobiol.* **54**, 8071–8089 (2017).
48. D. V. Hansen, J. E. Hanson, M. Sheng, Microglia in Alzheimer's disease. *J. Cell Biol.* **217**, 459–472 (2018).
49. M. K. Zabel, W. M. Kirsch, From development to dysfunction: microglia and the complement cascade in CNS homeostasis. *Ageing Res. Rev.* **12**, 749–756 (2013).
50. M. Wang, Y. Jiang, Z. Huang, Loss of C9orf72 in microglia drives neuronal injury by enhancing synaptic pruning in aged and Alzheimer's disease mice. *Neurosci. Bull.* **38**, 327–330 (2022).
51. N. Burnashev, H. Monyer, P. H. Seeburg, B. Sakmann, Divalent ion permeability of AMPA receptor channels is dominated by the edited form of a single subunit. *Neuron* **8**, 189–198 (1992).
52. S. G. Ancona Esselmann, J. Diaz-Alonso, J. M. Levy, M. A. Bemben, R. A. Nicoll, Synaptic homeostasis requires the membrane-proximal carboxy tail of GluA2. *Proc. Natl. Acad. Sci. U.S.A.* **114**, 13266–13271 (2017).
53. S. El-Boustani *et al.*, Locally coordinated synaptic plasticity of visual cortex neurons in vivo. *Science* **360**, 1349–1354 (2018).
54. D. Miyamoto, W. Marshall, G. Tononi, C. Cirelli, Net decrease in spine-surface GluA1-containing AMPA receptors after post-learning sleep in the adult mouse cortex. *Nat. Commun.* **12**, 2881 (2021).
55. H. L. Tan, R. H. Roth, A. R. Graves, R. H. Cudmore, R. L. Huganir, Lamina-specific AMPA receptor dynamics following visual deprivation in vivo. *Life* **9**, e52420 (2020).
56. A. J. Holtmaat *et al.*, Transient and persistent dendritic spines in the neocortex in vivo. *Neuron* **45**, 279–291 (2005).
57. H. Hsieh *et al.*, AMPAR removal underlies Abeta-induced synaptic depression and dendritic spine loss. *Neuron* **52**, 831–843 (2006).
58. S. Hong *et al.*, Complement and microglia mediate early synapse loss in Alzheimer mouse models. *Science* **352**, 712–716 (2016).
59. M. T. Heneka *et al.*, Neuroinflammation in Alzheimer's disease. *Lancet Neurol.* **14**, 388–405 (2015).
60. H. Sasaguri *et al.*, APP mouse models for Alzheimer's disease preclinical studies. *EMBO J.* **36**, 2473–2487 (2017).
61. Z. V. Guo *et al.*, Procedures for behavioral experiments in head-fixed mice. *PLoS One* **9**, e88678 (2014).
62. S. E. Kwon, H. Yang, G. Minamisawa, D. H. O'Connor, Sensory and decision-related activity propagate in a cortical feedback loop during touch perception. *Nat. Neurosci.* **19**, 1243–1249 (2016).
63. T. Komiyama *et al.*, Learning-related fine-scale specificity imaged in motor cortex circuits of behaving mice. *Nature* **464**, 1182–1186 (2010).
64. H. Ma *et al.*, Amygdala-hippocampal innervation modulates stress-induced depressive-like behaviors through AMPA receptors. *Proc. Natl. Acad. Sci. U.S.A.* **118**, e2019409118 (2021).
65. T. C. Harrison, A. Sigler, T. H. Murphy, Simple and cost-effective hardware and software for functional brain mapping using intrinsic optical signal imaging. *J. Neurosci. Methods* **182**, 211–218 (2009).